International Journal of Rock Mechanics & Mining Sciences 141 (2021) 104707

Contents lists available at ScienceDirect

International Journal of Rock Mechanics and Mining Sciences

journal homepage: http://www.elsevier.com/locate/ijrmms

Accurate moment tensor inversion of acoustic emissions and its application to Brazilian splitting test

Yi Ren [a], Václav Vavryčuk [b,*], Shunchuan Wu [a,c], Yongtao Gao [a]

[a] Key Laboratory of Ministry for Efficient Mining and Safety of Metal Mines, University of Science and Technology Beijing, Beijing, 100083, China
[b] Institute of Geophysics, Academy of Sciences of the Czech Republic, Boční II, 14131, Praha 4, Czech Republic
[c] Land Resources Engineering, Kunming University of Science and Technology, Kunming, 650093, Yunnan, China

ARTICLE INFO

Keywords:
Brazilian splitting test
Focal mechanism
Moment tensor
Sensor calibration
Tensile fracturing
Weighted least squares

ABSTRACT

The efficiency of three inversions for accurate moment tensors: (1) the standard least-squares inversion, (2) the weighted least-squares inversion, and (3) the shear-tensile-compressive (STC) source inversion, is tested on acoustic emissions (AEs) produced during the Brazilian splitting test. A comparison of plots of the P/T axes of the focal mechanisms reveals that the double-couple part of the moment tensors is well constrained for all three inversions. By contrast, diamond source-type plots show that the non-double-couple components of the retrieved moment tensors are more sensitive to errors due to neglecting inhomogeneities and anisotropy in the rock sample, near-field terms and other wave phenomena effects. The weighted inversion and the STC inversion work better than the standard least-squares method and yield less scattered results. If moment tensors of AEs contain significant non-double-couple components of moment tensors produced by non-shear fracturing, the STC inversion proved to be most accurate. The retrieved moment tensors are well consistent with the expected fracture mechanism of AEs in the Brazilian splitting specimen and provide a further guidance for studying rock fracture processes.

1. Introduction

Acoustic emission (AE) monitoring and other advanced monitoring techniques are introduced in rock laboratory tests to study the rock fracture process and fracture mechanisms. In loading experiments of rock samples, authors study AE characteristics, such as AE counts[1,2] and AE hits,[3,4] locations and their spatiotemporal clustering,[5–10] focal mechanisms, moment tensors and fracture mode of AEs,[5–20,22,23] and event rate and seismic energy release during loading.[13,24–26] For example, based on the triaxial compression test of the salt rock sample, Manthei[5] described the application of the AE monitoring to the rock fracture analysis, including the AE locations and the moment tensor (MT) analysis of microcracks generated during the loading process. The results show that the focal mechanisms of microfractures can well explain the stress state in the rock and the formation of fractures. Zhang et al.[6] applied the ultrasonic and AE monitoring to measuring the P-wave velocity in the Brazilian split test of the sandstone. They constructed a transversely isotropic velocity model that changed with time, and imaged a spatiotemporal evolution of the specimen damage and of the source rupture mechanisms. Falls et al.[11] analyzed the focal mechanisms, source characteristics, and the spatiotemporal distribution of AEs during the loading of a large Brazilian split sample. Ma et al.[12] conducted an acoustic emission simulation study of the Brazilian test using the Discrete Element Method. The AE location and magnitude were monitored during the whole process of the simulation to observe a crack initiation and the associated AE evolution. Moment tensors were calculated by the forces and motions of the particles and then were decomposed. They mentioned that AE events (microcracks) in the Brazilian test can be classified into explosive (tensile), shear and implosive sources. Explosive sources were found to dominate both in the total number and energy emission, followed by shear sources and finally implosive sources. Du et al.[13] carried out a series of rock tests including the Brazilian indirect tension test (BITT), three-point bending test (TPBT), modified shear test (MST) and uniaxial compression test (UCT) to investigate the AE characteristics and the crack classification during rock fracture. Dividing lines were proposed in the so-called AF-RA scatter plots to classify the tensile and shear cracks. The authors showed that most of AE signals generated in bending and tensile failures mainly produce tensile cracks with a low RA (ratio of rise time to amplitude) and with high peak frequencies (above 100 kHz). Petružálek et al.[14]

* Corresponding author.
E-mail address: vv@ig.cas.cz (V. Vavryčuk).

https://doi.org/10.1016/j.ijrmms.2021.104707
Received 9 June 2020; Received in revised form 27 January 2021; Accepted 9 March 2021
1365-1609/

analyzed the influence of the near-field effects of the rock sample on the Green's function. They show that the near-field effects are quite small and can be ignored at distance above three wavelengths. They performed a grid search and apply the least-squares nonlinear minimization method to obtain the shear-tensile-compression (STC) source model of AEs generated in the Westerly Granite under the uniaxial compression. They compared differences between the STC model and the MT model in the analysis of the rock fracture. Stierle et al.[22] showed that retrieved moment tensors critically depend on anisotropy and attenuation during triaxial compression experiments of a granite sample and that geometry of faulting in anisotropic rocks should be studied using the source tensors. They also compared the amplifications obtained from different calibration methods[19–21] and applied the network calibration[20,21] to the moment tensor inversion, which proved that the MT inversion applied to a large dataset of AEs can be utilized to provide information on attenuation parameters of the rock sample.

The MT inversion of AEs is not easy, because the recorded AE data are affected by many complex phenomena such as high-frequency noise, near-field effects, waveform attenuation and scattering, anisotropy of the rock sample and coupling effects between sensors and the sample. A common way, how to solve the majority of these difficulties, is to calibrate the sensors. The sensors are usually calibrated using the ultrasonic calibration[19,20] and/or the network calibration.[20–22] The ultrasonic calibration requires the incident angle of waves to the ultrasonic sensors to be uniformly distributed in the range of 0–90°. Under this condition, a reliable amplitude correction and relative calibration coefficients of sensors can be determined. Such calibration coefficients will be different for each ultrasonic test. The network calibration method requires a set of hundreds of AEs and calibrates each sensor separately by minimizing the root-mean squares (RMS) of predicted and observed amplitudes inverted for the AE moment tensors.

However, in actual AE tests, especially in the Brazilian splitting tests and in the rock direct shear tests, the sample size is small, and the distribution range of AEs is large. In these cases, the sensor calibration is not enough for retrieving accurate moment tensors, because other factors such as noise, the near-field effect, anisotropy, and waveform attenuation will cause the quality of different event waveforms recorded by sensors to vary and might introduce significant errors in the inversion. Consequently, some other more efficient approaches are needed to suppress large errors in MTs for some events. The smaller the rock sample, the more obvious this phenomenon.

In order to improve the accuracy of MTs, the efficiency of two methods is tested in this paper. Firstly, the MT inversion using the weighted least-squares method, called the 'weighted inversion', and secondly, the inversion for the shear-tensile-compressive (STC) source model, called the 'STC inversion'. Both the methods are applied to data from the Brazilian splitting test of the granite specimen and their efficiency is compared with the standard least-squares inversion. Differences in double-couple (DC) and non-double-couple (non-DC) components of the retrieved MTs are analyzed: (1) the DC components are studied by the distribution of the pressure/tension (P/T) axes, and (2) the non-DC components are studied using the diamond plot of the compensated linear vector dipole (CLVD) and the isotropic component (ISO).[27]

2. Theory

2.1. Moment tensor inversion

The moment tensor inversion is based on the following expression:

$$\mathbf{u} = \mathbf{G}\,\mathbf{M}, \tag{1}$$

where $\mathbf{G}$ is the $n \times 6$ Green's function space derivative matrix, which represents the response of the medium from the source to the sensor.

$$\mathbf{G} = \begin{bmatrix} G_1^{(1)} & G_2^{(1)} & G_3^{(1)} & G_4^{(1)} & G_5^{(1)} & G_6^{(1)} \\ G_1^{(2)} & G_2^{(2)} & G_3^{(2)} & G_4^{(2)} & G_5^{(2)} & G_6^{(2)} \\ \cdots & \cdots & \cdots & \cdots & \cdots & \cdots \\ G_1^{(n)} & G_2^{(n)} & G_3^{(n)} & G_4^{(n)} & G_5^{(n)} & G_6^{(n)} \end{bmatrix}, \tag{2}$$

$G_k^{(i)}$ is the element of the Green's function matrix for the i-th sensor:

$$\begin{aligned} &G_1^{(i)} = G_{1,1}^{(i)},\ G_2^{(i)} = G_{2,2}^{(i)},\ G_3^{(i)} = G_{3,3}^{(i)}, \\ &G_4^{(i)} = G_{2,3}^{(i)} + G_{3,2}^{(i)},\ G_5^{(i)} = G_{1,3}^{(i)} + G_{3,1}^{(i)}, \\ &G_6^{(i)} = G_{2,1}^{(i)} + G_{1,2}^{(i)}, \end{aligned} \tag{3}$$

$G_{p,m}^{(i)}$ is the amplitude measured along the x_m-axis produced by the point force directed along the x_p-axis, $\mathbf{m}$ is the moment vector composed of six independent components of moment tensor $\mathbf{M}$,

$$\mathbf{m} = [\,M_{11} \quad M_{22} \quad M_{33} \quad M_{23} \quad M_{13} \quad M_{12}\,]^T, \tag{4}$$

$\mathbf{u}$ is a $n \times 1$ vector, representing observed amplitudes at sensors, and n is the number of observed amplitudes for a given event.

When inverting equation (1), the least-square method is often used for calculating the moment tensor,

$$\mathbf{M} = \left(\mathbf{G}^T\mathbf{G}\right)^{-1}\mathbf{G}^T\mathbf{u}\,. \tag{5}$$

In order to check the accuracy of the obtained moment tensor, the normalized RMS difference between the observed and predicted amplitudes is calculated:

$$\mathrm{RMS} = \frac{\sqrt{\sum_{i=1}^{n}\left(u_i^{\mathrm{obs}} - u_i^{\mathrm{theor}}\right)^2}}{\sqrt{\sum_{i=1}^{n}\left(u_i^{\mathrm{obs}}\right)^2}}, \tag{6}$$

where i is the sensor sequential number, u_i^{obs} is the observed amplitude of the i-th sensor, and u_i^{theor} is the theoretical amplitude predicted at the i-th sensor. The smaller the RMS, the more accurate the moment tensor. The minimum number of inverted amplitudes is six but because of noise in data, more amplitudes are needed the inversion to be well overdetermined.

2.2. Weighted least-squares inversion

The simplest least-squares method treats the importance of each data point in the inversion equally. By contrast, the weighted least-squares estimation is a mathematical optimization technique that weights the original model parameters to make a new model with no heteroscedasticity, and it estimates its parameters.[28] If the positions and waveforms of events collected by the same sensor vary, different weight coefficients can be applied to the MT inversion in order to decrease/increase the role of the particular sensor in the inversion process. The formula for the weighted inversion reads as follows:

$$S = \sum_{i=1}^{n} W_i\left(u_i^{\mathrm{obs}} - u_i^{\mathrm{theor}}\right)^2 = \min, \tag{7}$$

where S is the sum of the squared residuals, which is minimized by the least-squares procedure, and W_i is the weight of the i-th sensor. If the weights of all sensors equal 1, it will be the ordinary least-squares method. Apparently, the selection of weights is a key issue for improving the efficiency of the least squares and here the Jackknife method is used to calculate the weights.

The Jackknife method[29] is a resampling method, the motivation of which is to reduce the deviation of the estimate of observations. This estimation is found by systematically leaving out each observation from the dataset and calculating each sub-estimate result. Then the impact of each observation on the overall result can be evaluated by comparing all the results.

Since the purpose is to obtain a low inversion error quantified by the RMS, then the RMS is used as a parameter for finding the weights by the Jackknife method. If the signals collected by all sensors are of high quality and consistent, the RMS obtained by ignoring one of the sensors will be small and close to the value obtained for all sensors. If the quality of some sensors is low (e.g., due to noise or near-field effects), ignoring or depressing any of these sensors can remarkably reduce the RMS. Therefore, the ratio W_i^j is chosen as the weighting coefficient:

$$W_i^j = \left(\frac{RMS_i^j}{RMS_{\max}^j}\right)^2, \tag{8}$$

where W_i^j is the weighting coefficient of the i-th sensor for the j-th event, which can reduce the role of the amplitude with a large RMS and improve the role of the amplitude with a small RMS in the calculation of moment tensors. The $RMS^j{}_{\max}$ is the maximum value of $RMS^j{}_i$ obtained by ignoring any sensor in event j.

The operation process is specified by the following steps:

Ignore the first sensor and use the remaining sensors to calculate the MT and the corresponding RMS of each event, $RMS^j{}_1$, where j is the event number;

Ignore the second sensor and use the remaining sensors to calculate the MT and the corresponding RMS of each event, $RMS^j{}_2$;

Repeat the procedure for the other sensors i and calculate the RMS for all events j, $RMS^j{}_i$;

Use the ratio W_i^j as the weighting coefficient of the i-th sensor of event j to form a weighting matrix:

$$W^j = \left[W_1^j \cdots\ W_i^j \cdots W_n^j\right] = \left[\left(\frac{RMS_1^j}{RMS_{\max}^j}\right)^2 \cdots \left(\frac{RMS_i^j}{RMS_{\max}^j}\right)^2 \cdots \left(\frac{RMS_n^j}{RMS_{\max}^j}\right)^2\right] \tag{9}$$

Introduce the weighting matrix (9) into formula (7) and calculate the new moment tensors and the corresponding RMS defined in formula (6).

The principle of the method is explained as follows. If the weighting coefficient W_i^j of the i-th sensor and j-th event is large, ignoring this coefficient will bring a large error into the MT inversion of event j. It means that the credibility of sensor i is high. Consequently, the sensor corresponding to $RMS^j{}_{\max}$ has the highest credibility. When one of sensors has an extremely poor quality, the weighting coefficient W_i^j will be close to 0. In this case, ignoring this sensor will significantly reduce the RMS. When the $RMS^j{}_i$ of all sensors are relatively small and similar, all the weighting coefficients W_i^j will be close to 1 and the weighting matrix will have a weak effect on the MT inversion of the event. When the $RMS^j{}_i$ difference between different sensors is large, the weighting matrix calculated using the ratios W_i^j will significantly deviate from the identity matrix and it will greatly improve the accuracy of the MT inversion.

The principle of calculating weights from the RMS distributions is demonstrated in Fig. 1, where all analyzed events are divided into three basic types. Event type 1 represents an event, where the P-wave amplitudes are of a high quality at all sensors. Consequently, ignoring individual sensors does not affect the RMS too much. This situation is considered as optimum. Event type 2 represents an event, for which one of the sensors (Fig. 1, sensor 8, blue dot) is of a poor quality and produces a biased P-wave amplitude. The other sensors acquire a good waveform quality. Ignoring the sensor with a biased P-wave amplitude can significantly reduce the inversion error of this event. Event type 3 represents an event, for which several sensors are of a low quality and produce biased amplitudes (Fig. 1, sensors 1 and 9, black triangles). Even if the sensor with the lowest acquisition quality is ignored, the obtained moment tensor is still unstable, because ignoring other sensors can also greatly reduce the RMS.

2.3. Shear-tensile-compressive source (STC) inversion

Another possibility how to achieve more accurate moment tensors determined from noisy data is reducing the number of inverted parameters and thus stabilizing the inversion process. Instead of calculating six parameters of the moment tensor, it is possible to invert for four parameters only, if AEs are produced by shear cracks. Alternatively, it is possible to invert for five parameters, if AEs combine shear and tensile/compaction fracturing described by the STC source model proposed by Vavryčuk[30] (see Fig. 2).

For the STC cracks, the slip vector **u** does not lie in the fault. The source is described by four angles: strike ϕ, dip δ, rake λ and slope α. Strike ϕ and dip δ define the orientation of the crack, rake λ and slope α define the direction $\boldsymbol{\nu}$ of slip **u** (see Fig. 3). The slope α is defined as the deviation of the slip vector **u** from the crack. The slope angle α is positive

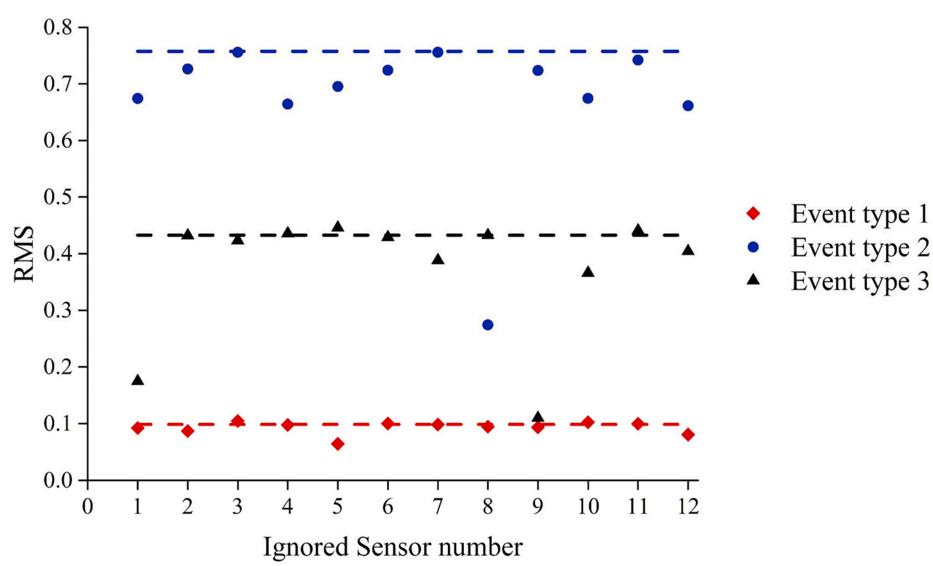

Fig. 1. Examples of three types of AE events with different RMS distributions; the red dashed line represents the RMS obtained by the inversion of the moment tensor using all sensors for Event type 1; the blue dashed line is for Event type 2; the black dashed line is for Event type 3. (For interpretation of the references to color in this figure legend, the reader is referred to the Web version of this article.)

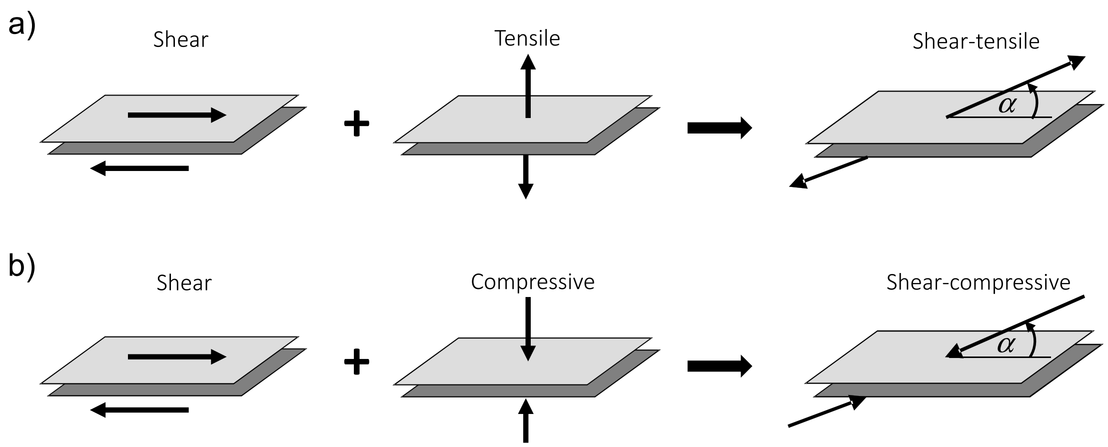

Fig. 2. Scheme of the shear-tensile (a) and shear-compressive (b) events. The slope α is defined as the angle between the slip vector and the plane of the crack; it is positive for shear-tensile sources and negative for shear-compressive sources.

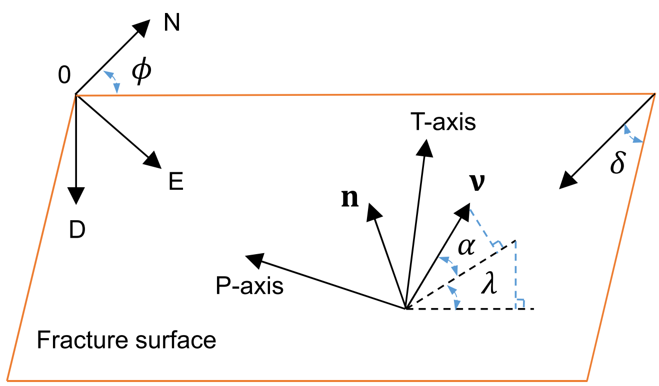

Fig. 3. Definition of strike ϕ, dip δ, rake λ and slope α describing geometry of the STC model. Vector **n** and $\boldsymbol{\nu}$ are the normal to the fracture surface and the slip direction, respectively. N - North, E – East, D – Down. O is the origin of the coordinate system.

for the shear-tensile fracturing and negative for the shear-compressive fracturing. The fault normal **n** and the direction vector $\boldsymbol{\nu}$ of slip **u** are expressed for the STC sources in terms of angles ϕ, δ, λ and α as follows[31]:

$$\begin{aligned} n_1 &= -\sin\delta\sin\varphi\,, \\ n_2 &= \sin\delta\cos\varphi\,, \\ n_3 &= -\cos\delta\,, \end{aligned} \tag{10}$$

$$\begin{aligned} \nu_1 &= (\cos\lambda\cos\varphi + \cos\delta\sin\lambda\sin\varphi)\cos\alpha - \sin\delta\sin\varphi\sin\alpha\,, \\ \nu_2 &= (\cos\lambda\sin\varphi - \cos\delta\sin\lambda\cos\varphi)\cos\alpha + \sin\delta\cos\varphi\sin\alpha\,, \\ \nu_3 &= -\sin\lambda\sin\delta\cos\alpha - \cos\delta\sin\alpha\,, \end{aligned} \tag{11}$$

The moment tensor **M** is expressed for isotropic rocks as[30,31]:

$$M_{ij} = uS\left(\lambda n_k \nu_k \delta_{ij} + \mu n_i \nu_j\right)\,, \quad i, j \; = \; 1,\; 2,\; 3, \tag{12}$$

where u is the slip, S is the crack area, λ and μ are the Lamé's coefficients, and δ_{ij} is the Kronecker delta. The Einstein summation rule is used over index k.

While the weighted inversion for the moment tensor is linear, performed in one step or in several iterations, the STC inversion is nonlinear. It can be performed by standard optimization methods, when the sum of the absolute differences between theoretical and observed amplitudes are minimized. The most common approaches are: (1) the simplex algorithm and its extensions designed for the linear programming, (2) iterative methods such as the conjugate gradient method, or (3) the stochastic methods such as the Monte Carlo method. For a low number of optimization parameters, the grid search over the parameter space is also frequently used.

In tests of the efficiency of the MT inversions in section Results, a solver of the constrained nonlinear multivariable function available in the Matlab package was adopted. This solver is based on the 'interior-point algorithm', which uses the conjugate gradient method and finds a minimum in iterations and within prescribed limits.[32] The limits were set as follows: $0 \le \varphi \le 360^\circ$, $0 \le \delta \le 90^\circ$, $-180^\circ \le \lambda \le 180^\circ$, $-90^\circ \le \alpha \le 90^\circ$, and $-0.3 \le \lambda/\mu \le 15$. For the initial guess of the solution, the strike, dip and rake angles obtained from the DC part of the moment tensors calculated by the standard least-squares inversion were used. For positive/negative ISO components, the slope α was set $+20^\circ/-20^\circ$, respectively. The procedure was fast and produced mostly the same results as the more time-consuming grid-search method.

3. Setup of the experiment

A computer-controlled servo-hydraulic compression system with a maximum load capacity of 2000 kN was used for loading. The AE monitoring is performed by the InSiteLab AE signal acquisition system (see Fig. 4a) provided by ITASCA and by the Nano30 sensors provided by the American Physical Acoustics (PAC), as shown in Fig. 4. The InSiteLab acquisition system uses a PAD amplifier unit with a built-in 100 kHz - 1 MHz bandpass filter for amplifying the original AE signal with a gain value of 30–70 dB, and for transmitting and saving the signal. The sampling frequency is 10 MHz, and the digital resolution of the waveforms is 16 bit. The Nano30 sensors have a diameter of ~8 mm and an operating frequency range of 125–750 kHz. In addition, the Pulser Interface Unit (PIU) can send a 500 V pulse to each sensor acting as an active source event. The other sensors can be used as receivers to record the signals and to construct the P-wave velocity models, needed for the calculation of AE locations and for the inversion of the moment tensors. Since this device cannot conduct the ultrasonic testing and the AE monitoring simultaneously, the ultrasonic speed measurement was not conducted during the test, but multiple sets of ultrasonic data were tested before the test. The P-wave velocity was measured for a ray passing through the center of symmetry of the sample and varied between 4300 m/s and 4700 m/s. The median value of 4500 m/s was used for locating AEs and for the MT inversion.

Six granite specimens taken from Laiyang, Shandong Province, China, were tested. The uniaxial compressive strength of this kind of granite is about 150 MPa, the density is 2.647 g/cm^3, the specimens are composed of quartz (35%), feldspar (60%) and other mineral particles (5%). According to the ISRM[33] recommended method, the samples are processed into a disc shape with a size of Φ50 mm × 25 mm with no large cracks on the surface and with a flat end face. The non-parallelism

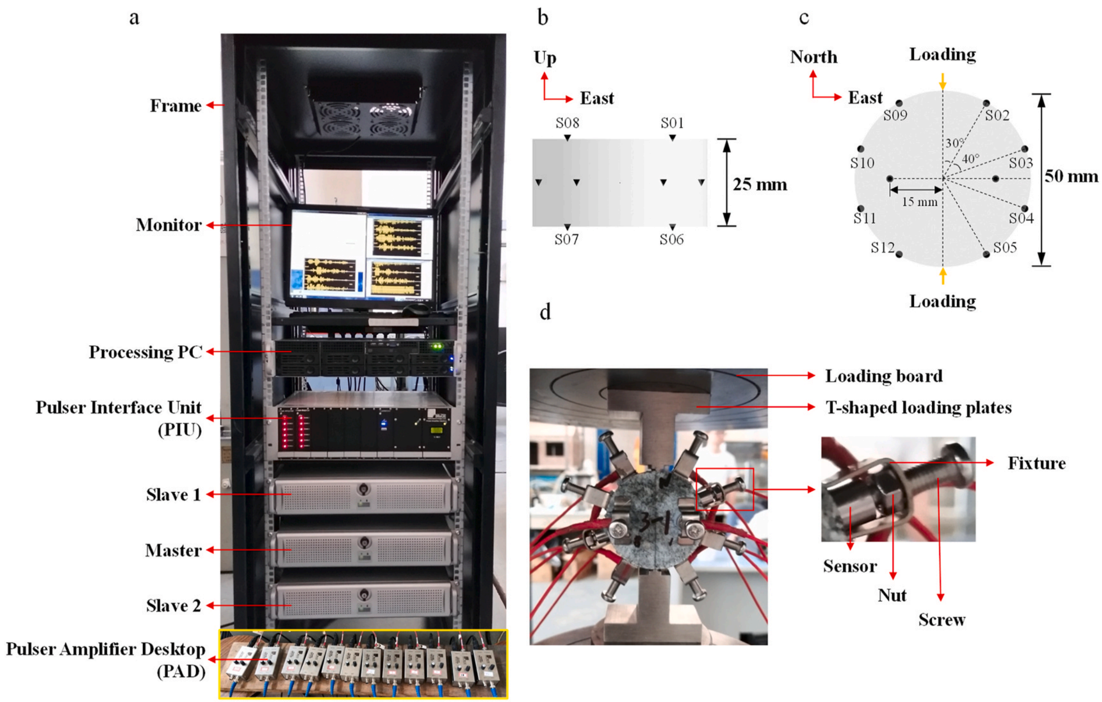

Fig. 4. Schematic diagram of AE monitoring and loading experimental setup. (a): AE monitoring device, Frame, Monitor, Processing PC, Pulser Interface Unit (PIU), Pulser Amplifier Desktop (PAD), Slave 1 and Master and Slave 2: continuous acquisition system. (b): Up-East view of sensors layout. (c): North-East view of sensors layout and loading directions. (d): Photograph of loading device and sensor installation details.

of the upper and lower end surfaces of the sample is less than 0.02 mm. Silicone grease is applied between the AE sensors and the sample to reduce the signal attenuation. The sensors are fixed using a designed fixture and screws were used to maintain a constant contact pressure,[34] which is essential for obtaining undistorted amplitudes. The designed fixture is fixed on the surface of the specimen with glue. The sensor layout and the AE coordinate system are shown in Fig. 4b and c. Since the analysis results of 6 specimens are similar, only one of the specimens numbered 3–1 is taken here for display and analysis. In order to conveniently install more AE sensors, the linear loading method was chosen. Two 2.1 mm wide[35] flat steel bars were placed between the two notched T-shaped loading plates and the specimen for loading (see Fig. 4d). The loading speed is 20 N/s.

4. Results

4.1. Source location and selection of suitable AEs

The test lasted for a total of 787.7 s (the time span between the first and last AE event recorded), and the tensile strength[36] of the obtained sample was 9.55 MPa. The results of the sample fracturing are shown in Fig. 5a–b. Based on the velocity model obtained by ultrasonic testing, the AE events were located using the collapsing grid search algorithm,[37] and a total of 1606 effective source events with at least 4 P-wave arrivals were obtained, as shown in Fig. 5c–e. In order to obtain high-quality moment tensors, the following criteria were applied for selecting the analyzed events:

The number of the P-wave amplitudes is 12.

The signal-to-noise ratio (SNR) is higher than 10.

The location error is within 2 mm, which is calculated by the expression:

$$E_{\mathrm{RMS}} = V_p \sqrt{\frac{\sum_{i=1}^{N} \Delta T_i}{N}}, \tag{13}$$

where V_p is the P-wave velocity, N is the number of P-wave arrivals, ΔT_i is the difference between the measured arrival time and the theoretical time predicted by the location procedure.

All sensors have a minimum distance greater than 10 mm from the AE location.

The distance of the AE location from the cylindrical surface and flat surface is greater than 5 mm and 2.5 mm, respectively.

As a result, a total of 156 AE events meeting the required standards were selected. The limitation of the distance between the sensor and the AE location is needed to reduce the influence of the near-field effects on the moment tensor inversion. The limitation of the AE location is needed to ensure the event to have a reasonable sensor layout on the focal sphere and to suppress an interaction of emitted waves with the free surface of the sample. The temporal and spatial distributions of the selected events are shown in Fig. 5f–h.

Fig. 5c–h shows that the AEs appear first at the margin of the sample in the north-south direction, which is near the loading position of the T-shaped loading plate. This is mainly because the linear loading is prone to generate a stress concentration at the contact surface, resulting in many AEs. As the loading progresses, the locations of AEs migrate towards the center of the disc, which eventually leads to the rupture of the specimen.

4.2. Moment tensor inversion

The quality and properties of calculated moment tensors using the standard inversion, the weighted inversion, and the STC inversion, respectively, are assessed by plots of the P/T axes (Fig. 6, upper panels). and by the diamond CLVD-ISO source-type plots (Fig. 6, lower panels). The analysis of the P/T axes of AEs is widely used,[14–16,20,22] because accurate P/T axes should form separated and well-defined clusters, which reflect the stress state in the sample.[38] Consequently, highly scattered P/T clusters, which mutually overlap, often indicate uncertainties in the moment tensors. On the other hand, the diamond CLVD-ISO plot[27] shows the composition of each component (DC, CLVD and ISO[27,30,31]) in the moment tensor and points to the character of fracturing of AEs. Predominantly shear events are located close to the

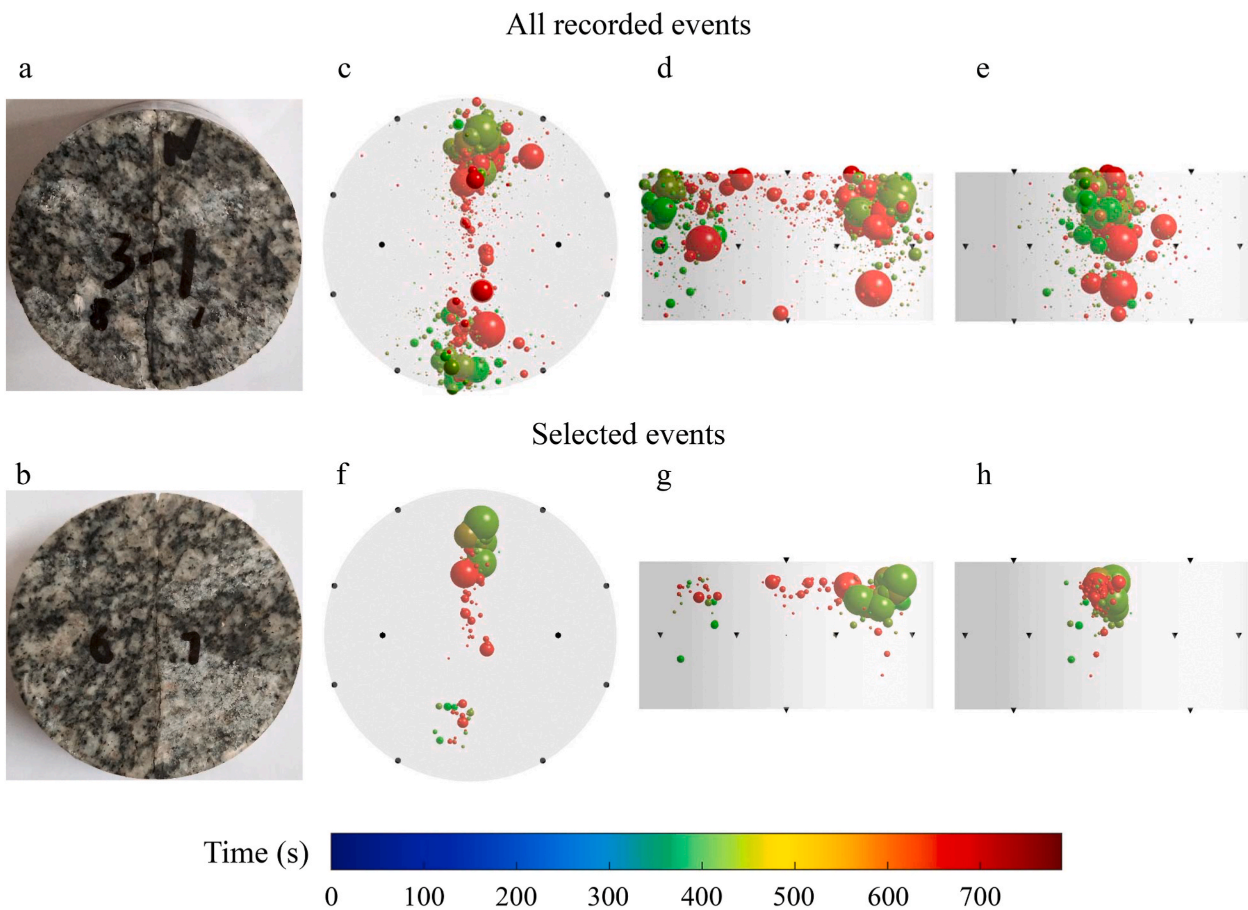

Fig. 5. (a) and (b): The fracture observed for the disc sample after the failure; (c)–(e): the distribution and SNR (diameter of the event ball) of all observed AEs in North-East view and Up-North view and Up-East view; (f)–(h): the distribution and SNR of the events selected for the moment tensor inversion in North-East view and Up-North view and Up-East view. The time of AEs is color coded. (For interpretation of the references to color in this figure legend, the reader is referred to the Web version of this article.)

origin and highly non-shear events are at the margins of the plot. The percentage of the DC component is indicated by the color intensity at the source location in the diamond plot. Tensile AEs are characterized by positive CLVD and ISO components, while the compressive AEs have both CLVD and ISO negative. If the CLVD and ISO are of different signs, the rock sample is either significantly anisotropic or the retrieved MTs suffer from large errors.

Upper panels in Fig. 6 show the distributions of the P/T axes for all three inversions. The P axes form compact clusters and only a few events display P-axes in spurious directions close to the axis of the disc (i.e., points in the area close to the center of the circle). Under the ideal linear loading state and the completely homogeneous medium, the P axes of AEs should be close to the loading direction and thus they should be concentrated in the upper and lower ends of the P/T plot, which is the north-south direction. The T axes should mostly be concentrated in the left and right ends of the P/T plot, which is the east-west direction. The observed P axes of the events generated in this experiment are mostly distributed in the north-south direction with only a few anomalous events distributed in other directions. By contrast, the distribution of T axes is more complicated. The T axes are more scattered and form basically two main clusters: one cluster distributed in the east-west direction and the other cluster along the disc axis (the area located near the center of the plot). The reasons for deviations of the P/T axes from the expected distribution are as follows: (1) The heterogeneity of the rock sample might cause irregularities in the stress, which becomes different from the ideal state. Therefore, the distribution of the P and T axes can deviate from the ideal state; (2) The loading method used in this test is not actually an ideal linear load, but a slender surface load. Therefore, tensile stress can appear in all directions perpendicular to the loading direction. Consequently, the T axes are distributed not only in the east-west direction, but a portion of AEs have T axes concentrated in the direction along the disc axis.

When comparing patterns of the P/T axes for the three inversions in Fig. 6, one can see that their differences are minor. It means that neither the weighted inversion nor the STC inversion improves significantly the DC part of the moment tensors. This confirms that the DC components are usually well constrained compared to the non-DC components, the determination of which is more data demanding, and thus they are more sensitive to the errors of the inversion.

Lower panels in Fig. 6 show the diamond CLVD-ISO plots with the color-coded time for the three different MT inversions. The MTs calculated by the standard inversion are very scattered in the CLVD-ISO plot, which indicates high numerical errors produced by the inversion. Consequently, the non-DC components cannot be interpreted well in terms of their rupture mechanism. Nevertheless, it can be seen that many compressive events and a small portion of tensile events are produced in the beginning of loading. At later stages, the number of tensile events gradually increases, and finally the sample produces the overall tensile failure. When using the weighted inversion, the scatter of events is visibly reduced in the CLVD-ISO plot (Fig. 6, lower central plot). The compressive events with negative ISO and CLVD form a more compact cluster and the events with the predominant DC (the area in the center of the diamond) are less frequent. Also, the tensile events with positive ISO and CLVD seem to be less scattered. The clustering of compressive and tensile events is even more visible for MTs calculated by the STC inversion. This inversion is *apriori* constrained to produce the

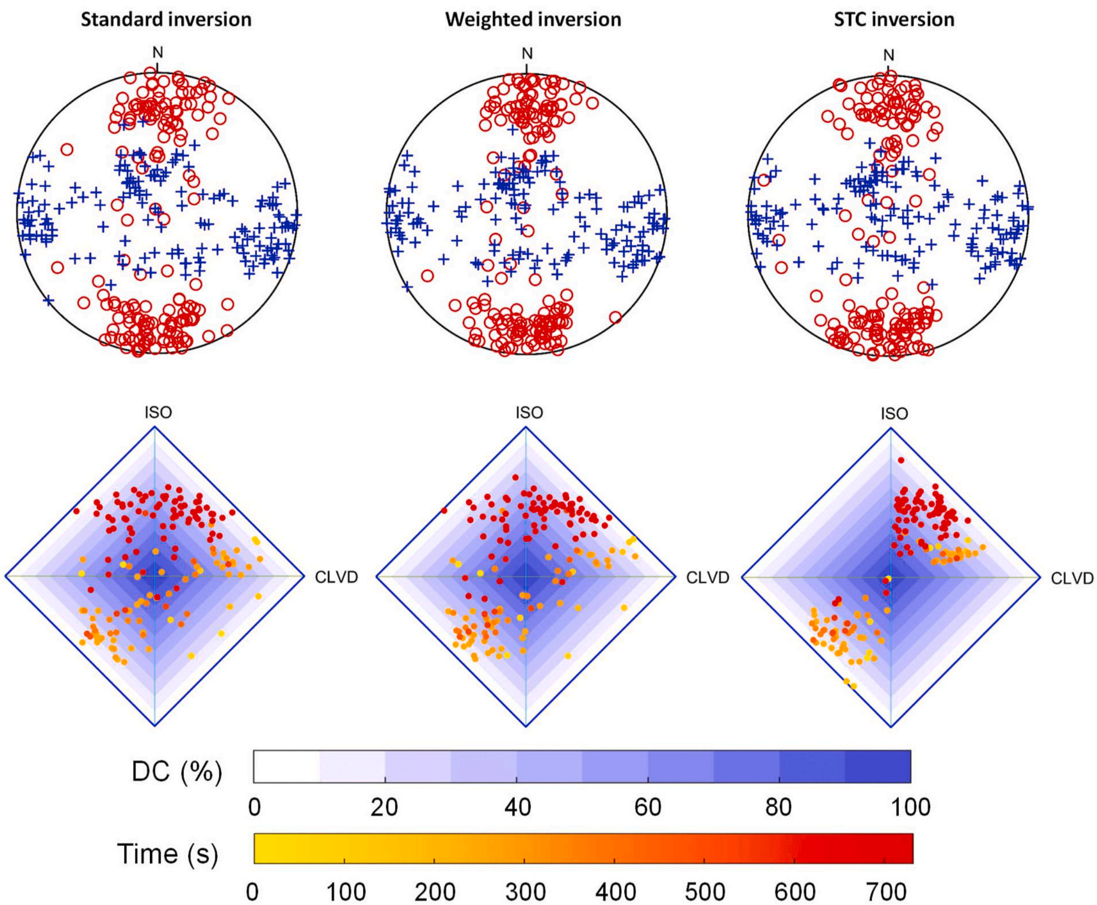

Fig. 6. Plots of the P/T axes on the focal sphere (upper panels) and the diamond CLVD-ISO plots (lower panels) for moment tensors of 156 AEs under study. The moment tensors were calculated using the standard (left), weighted (middle) and STC (right) inversions. The P and T axes are marked by red circles and blue plus signs, respectively. The color scale in the diamond CLVD-ISO plots shows time in seconds. The ISO and CLVD percentages are calculated according to equations 6–10 of Vavryčuk.[27] (For interpretation of the references to color in this figure legend, the reader is referred to the Web version of this article.)

ISO and CLVD components of the same sign. Since this constraint is physically reasonable, it helps considerably to reduce the errors of the non-DC components. Hence the STC inversion proved to be clearly superior for getting accurate non-DC components of MTs.

As regards the time evolution, tensile and compressive events coexist in both the early and middle periods of the experiment, while the latter periods are dominated by tensile events and the number of compressive events is reduced. Only few shear events are observed during the whole test. Fig. 5c–h shows that the observed initially activated cracks are not near the center of the disc. This phenomenon is different from the theoretical prediction based on the Griffith criterion. The main reason for this phenomenon is the unevenness of the sample and a local concentration of stress.

The above conclusions about the efficiency of the three inversions is confirmed by the analysis of the most stable and accurate moment tensors of AEs, which are shown in Fig. 7. Here, only 50% of events with the lowest RMS are displayed. Again, the P/T axes plots are essentially the same for all three inversions. In addition, the clustering of the T axes is now more visible. This proves that the T-cluster along the axis of the disc was not spurious, but it reflects true properties of the AEs. Also, the improvement of the efficiency of the weighted and STC inversions, when calculating the non-DC components, is well identified. As for the full dataset, the STC inversion manifests its superiority and yields results, which can be physically well interpreted.

Finally, Fig. 8 shows the estimated errors of the 78 most accurate MTs determined by the STC inversion and shown in Fig. 7 (right-hand panels). These errors are calculated by repeating inversions of data superimposed by random noise. The maximum noise level was 30% of the P-wave amplitude detected for the AEs at each sensor. The probability distribution was flat and the number of realizations of random noise was 100. The errors in the P/T axes are evaluated by the mean deviation of the noisy solutions from the true noise-free solution. The errors in the ISO and CLVD percentages are evaluated by the standard error of the 100 values of the ISO and CLVD of the noisy moment tensors. The figure indicates that the P-axes errors are mostly 5° being almost twice more accurate than the T axes with the errors of about 10°. The ISO component is determined with a predominant error of about 4%, while the CLVD component has a predominant error of about 15%. The higher errors of the CLVD compared to the ISO are observed quite frequently in earthquakes source studies[31] being caused by a more complicated radiation pattern of the CLVD source than of the ISO source, which produces a uniform radiation in all directions.

5. Discussion and conclusions

Since only a limited number of AE sensors is used for monitoring, it is desirable to suppress errors produced by low-quality sensors and by other factors neglected in the inversion, because the procedure becomes unstable and not well overdetermined. The MT inversion can easily introduce large errors for AEs observed in the rock laboratory, in particular, for small rock samples with a complicated structure. The standard approach for improving the accuracy of MTs is to apply a network calibration, which quantifies coupling effects between sensors and the rock, and identifies incorrectly calibrated sensors. However, the retrieved MTs are sometimes unstable and display a large scatter even after a proper sensor calibration. In such cases, some other tools must be

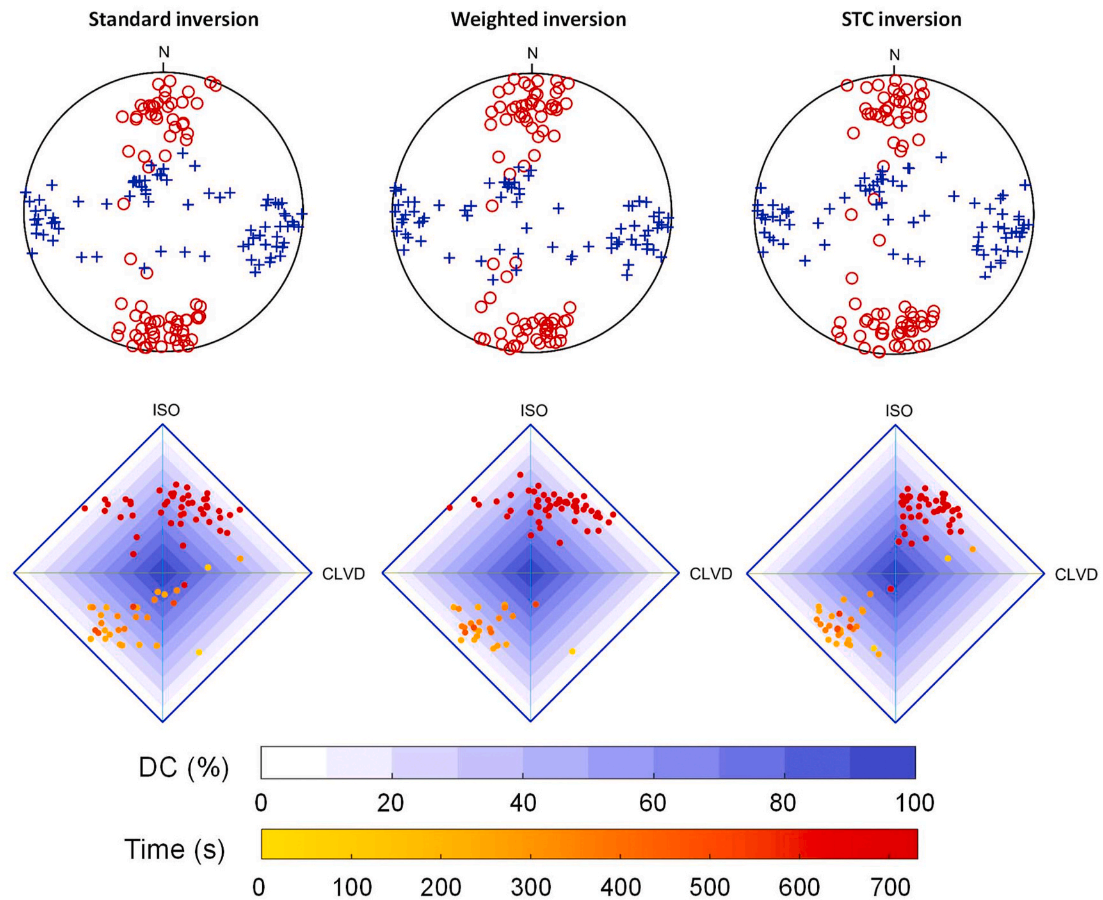

Fig. 7. Plots of the P/T axes on the focal sphere (upper panels) and the diamond CLVD-ISO plots (lower panels) for 78 most accurate moment tensors under study. Fore details, see the caption of Fig. 6.

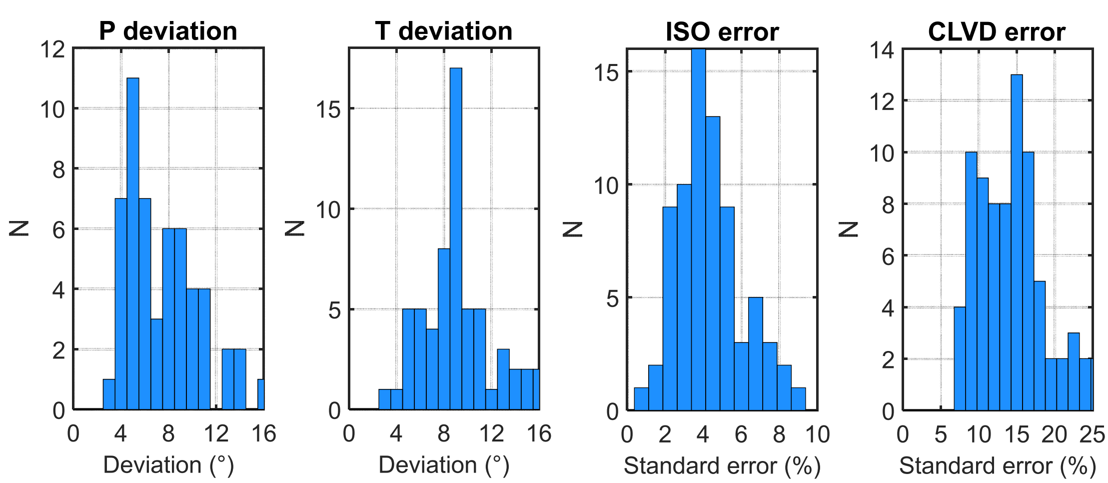

Fig. 8. Histograms of estimated errors of the P/T axes and the ISO and CLVD components for 78 most accurate moment tensors calculated using the STC inversion.

applied to improve the accuracy of the calculated MTs.

The weighted inversion described in Section 2.2 can help with this goal and can improve the accuracy of the MTs. If the number of sensors used in experiments is large, the selection procedure of high quality measurements can be run repeatedly in iterations, in order to obtain a more realistic weighting matrix and more accurate moment tensors. Another possibility is to employ the STC inversion described in Section 2.3 provided that the analyzed AEs contain significant non-DC components produced by non-shear fracturing. The weighted and STC inversions are applicable even to a small number of events, which have a rather wide range of magnitudes and locations. They can also be used in studies of AEs in anisotropic rocks, if the Green's function is properly calculated.[22,39–41] The analysis proved that the diamond CLVD-ISO plot of AEs corresponding to these inversions is more consistent than that corresponding to the standard inversion, and the retrieved MTs can reasonably explain the properties of the fracture process and failure mechanism of the rock specimen.

The events selected for the inversion of the moment tensors have a relatively high signal-to-noise ratio, which can roughly explain the rupture process of the sample. However, the number of the events selected for the MT analysis and the number of effectively located events are still relatively small compared to the whole set of events. In particular, most of the events located in this experiment are distributed in the upper side of the disc. Only few events are located in the lower side. Therefore, the MTs cannot represent properly the whole process of the specimen rupture. In future, it is desirable to analyze more extensive datasets of events with a high number and a high quality of the P-wave picks. The processing of such datasets can provide a more reliable test of the accuracy of MTs determined using the weighted and STC inversions and their interpretation can help in deeper understanding of the rock failure mechanism.

Declaration of competing interest

The authors declare that they have no known competing financial interests or personal relationships that could have appeared to influence the work reported in this paper.

Acknowledgements

We would like to thank the editors and two anonymous reviewers for their helpful comments and suggestions. The work was partially supported by the Czech Science Foundation, grant No. 19-06422S and by the scholarship provided by the China Scholarship Council to the first author, and by National Natural Science Foundation of China (51934003, 51774020). The diamond CLVD-ISO plots were produced by the publicly available Matlab package MT-DECOMPOSITION (https://www.ig.cas.cz/mt-decomposition/).

References

1 Li C, Nordlund E. Experimental verification of the Kaiser effect in rocks. *Rock Mech Rock Eng*. 1993;26(4):333–351. https://doi.org/10.1007/BF01027116.
2 Zhang SW, Shou KJ, Xian XF, Zhou JP, Liu GJ. Fractal characteristics and acoustic emission of anisotropic shale in Brazilian tests. *Tunn Undergr Space Technol*. 2018;71: 298–308. https://doi.org/10.1016/j.tust.2017.08.031.
3 Su GS, Shi YJ, Feng XT, Jiang JQ, Zhang J, Jiang Q. True-Triaxial experimental study of the evolutionary features of the acoustic emissions and sounds of rockburst processes. *Rock Mech Rock Eng*. 2018;51(2):375–389. https://doi.org/10.1007/s00603-017-1344-6.
4 Meng F, Wong LNY, Zhou H, Yu J, Cheng G. Shear rate effects on the post-peak shear behaviour and acoustic emission characteristics of artificially split granite joints. *Rock Mech Rock Eng*. 2019;52(7):2155–2174. https://doi.org/10.1007/s00603-018-1722-8.
5 Manthei G. Characterization of acoustic emission sources in a rock salt specimen under triaxial compression. *Bull Seismol Soc Am*. 2005;95(5):1674–1700. https://doi.org/10.1785/0120040076.
6 Zhang S, Wu S, Zhang G, Guo P, Chu C. Three-dimensional evolution of damage in sandstone Brazilian discs by the concurrent use of active and passive ultrasonic techniques. *Acta Geotech*. 2020;15:393–408. https://doi.org/10.1007/s11440-018-0737-3.
7 Zang A, Wagner FC, Stanchits S, Dresen G, Andresen R, Haidekker MA. Source analysis of acoustic emissions in Aue granite cores under symmetric and asymmetric compressive loads. *Geophys J Int*. 1998;135:1113–1130. https://doi.org/10.1046/j.1365-246X.1998.00706.x.
8 Graham CC, Stanchits S, Main IG, Dresen G. Comparison of polarity and moment tensor inversion methods for source analysis of acoustic emission data. *Int J Rock Mech Min Sci*. 2010;47:161–169. https://doi.org/10.1016/j.ijrmms.2009.05.002.
9 Thompson B, Young R, Lockner D. Premonitory acoustic emissions and stick-slip in natural and smooth-faulted Westerly granite. *J Geophys Res*. 2009;114. https://doi.org/10.1029/2008JB005753. B02205.
10 Chang SH, Lee CI. Estimation of cracking and damage mechanisms in rock under triaxial compression by moment tensor analysis of acoustic emission. *Int J Rock Mech Min Sci*. 2004;41(7):1069–1086. https://doi.org/10.1016/j.ijrmms.2004.04.006.
11 Falls SD, Young RP, Chow T, Hutchins DA. Acoustic emission analyses and tomographic velocity imaging in the study of failure in Brazilian disk tests. In: *The 30th US Symposium on Rock Mechanics (USRMS)*. Morgantown; 19-22 June 1989: 647–654.
12 Ma J, Wu S, Zhang XP, Gan Y. Modeling acoustic emission in the Brazilian test using moment tensor inversion. *Comput Geotech*. 2020;123:103567. https://doi.org/10.1016/j.compgeo.2020.103567.
13 Du K, Li X, Tao M, Wang S. Experimental study on acoustic emission (AE) characteristics and crack classification during rock fracture in several basic lab tests. *Int J Rock Mech Min Sci*. 2020;133:104411. https://doi.org/10.1016/j.ijrmms.2020.104411.
14 Petružálek M, Jechumtálová Z, kajíček T, et al. Acoustic emission in a laboratory: mechanism of microearthquakes using alternative source models. *J Geophys Res*. 2018;123(6):4965–4982. https://doi.org/10.1029/2017JB015393.
15 Petružálek M, Jechumtálová Z, Onysko R, et al. Application of the shear-tensile source model to acoustic emissions in Westerly granite. *Int J Rock Mech Min Sci*. 2020;128:104246. https://doi.org/10.1016/j.ijrmms.2020.104246.
16 Aker E, Kühn D, Vavryčuk V, Soldal M, Oye V. Experimental investigation of acoustic emissions and their moment tensors in rock during failure. *Int J Rock Mech Min Sci*. 2014;70:286–295. https://doi.org/10.1016/j.ijrmms.2014.05.003.
17 Sellers EJ, Kataka MO, Linzer LM. Source parameters of acoustic emission events and scaling with mining-induced seismicity. *J Geophys Res*. 2003;108(B9):1–16. https://doi.org/10.1029/2001JB000670. ESE7.
18 Pettitt WS, King MS. Acoustic emission and velocities associated with the formation of sets of parallel fractures in sandstones. *Int J Rock Mech Min Sci*. 2004;41:151–156. https://doi.org/10.1016/j.ijrmms.2003.12.043.
19 Kwiatek G, Charalampidou E-M, Dresen G, Stanchits S. An improved method for seismic moment tensor inversion of acoustic emissions through assessment of sensor coupling and sensitivity to incidence angle. *Int J Rock Mech Min Sci*. 2014;65: 153–161. https://doi.org/10.1016/j.ijrmms.2013.11.005.
20 Davi R, Vavryčuk V, Charalampidou E-M, Kwiatek G. Network sensor calibration for retrieving accurate moment tensors of acoustic emissions. *Int J Rock Mech Min Sci*. 2013;62:59–67. https://doi.org/10.1016/j.ijrmms.2013.04.004.
21 Davi R, Vavryčuk V. Seismic network calibration for retrieving accurate moment tensors. *Bull Seismol Soc Am*. 2012;102(6):2491–2506. https://doi.org/10.1785/0120110344.
22 Stierle E, Vavryčuk V, Kwiatek G, Charalampidou E-M, Bohnhoff M. Seismic moment tensors of acoustic emissions recorded during laboratory rock deformation experiments: sensitivity to attenuation and anisotropy. *Geophys J Int*. 2016;205(1): 38–50. https://doi.org/10.1093/gji/ggw009.
23 Kwiatek G, Martínez-Garzón P, Bohnhoff M. HybridMT: a MATLAB/shell environment package for seismic moment tensor inversion and refinement. *Seismol Res Lett*. 2016;87(4):964–976. https://doi.org/10.1785/0220150251.
24 Goebel THW, Becker TW, Scho, Dresen G, et al. Identifying fault heterogeneity through mapping spatial anomalies in acoustic emission statistics. *J Geophys Res*. 2012;117(B3):B03310.1–B03310.18. https://doi.org/10.1029/2011JB008763.
25 Backers T, Stanchits S, Dresen G. Tensile fracture propagation and acoustic emission activity in sandstone: the effect of loading rate. *Int J Rock Mech Min Sci*. 2005;42 (7–8):1094–1101. https://doi.org/10.1016/j.ijrmms.2005.05.011.
26 Lockner DA, Byerlee JD, Kuksenko V, Ponomarev A, Sidorin A. Quasi-static fault growth and shear fracture energy in granite. *Nature*. 1991;350(6313):39–42. https://doi.org/10.1038/350039a0.
27 Vavryčuk V. Moment tensor decomposition revisited. *J Seismol*. 2015;19(1):231–252. https://doi.org/10.1007/s10950-014-9463-y.
28 Mandel J. *The Statistical Analysis of Experimental Data*. New York: Interscience; 1964.
29 Quenouille MH. Problems in plane sampling. *Ann Math Stat*. 1949;20(3):355–375. https://doi.org/10.1214/aoms/1177729989.
30 Vavryčuk V. Inversion for parameters of tensile earthquakes. *J Geophys Res*. 2001; 106(8):16339–16355. https://doi.org/10.1029/2001JB000372.
31 Vavryčuk V. Tensile earthquakes: theory, modeling and inversion. *J Geophys Res*. 2011;116. https://doi.org/10.1029/2011JB008770. B12320.
32 Byrd RH, Gilbert JC, Nocedal J. A trust region method based on interior point techniques for nonlinear programming. *Math Program*. 2000;89(1):149–185. https://doi.org/10.1007/s101070000189.
33 Ulusay R. *The ISRM Suggested Methods for Rock Characterization, Testing and Monitoring: 2007-2014*. Springer; 2014.
34 Goodfellow SD, Tisato N, Ghofranitabari M, Nasseri MHB, Young RP. Attenuation properties of Fontainebleau sandstone during true-triaxial deformation using active and passive ultrasonics. *Rock Mech Rock Eng*. 2015;48(6):2551–2566. https://doi.org/10.1007/s00603-015-0833-8.
35 Hondros G. The evaluation of Poisson's ratio and the modulus of materials of low tensile resistance by the Brazilian (indirect tensile) test with particular reference to concrete. *Aust J Appl Sci*. 1959;10(3):243–268.
36 Bieniawski ZT, Hawkes I. Suggested methods for determining tensile strength of rock materials. *Int J Rock Mech Min Sci*. 1978;15(3):99–103.
37 Pettitt WS, Young RP. *InSite Seismic Processor–User Operations Manual Version 2.14*. Shrewsbury, UK: Applied Seismology Consultants; 2007.
38 Vavryčuk V. Principal earthquakes: theory and observations from the 2008 west bohemia swarm. *Earth Planet Sci Lett*. 2011;305:290–296. https://doi.org/10.1016/j.epsl.2011.03.002.
39 Vavryčuk V. Elastodynamic and elastostatic Green tensors for homogeneous weak transversely isotropic media. *Geophys J Int*. 1997;130:786–800. https://doi.org/10.1111/j.1365-246X.1997.tb01873.x.
40 Vavryčuk V. Ray velocity and ray attenuation in homogeneous anisotropic viscoelastic media. *Geophysics*. 2007;72(6):D119–D127. https://doi.org/10.1190/1.2768402.
41 Vavryčuk V. Velocity, attenuation and quality factor in anisotropic viscoelastic media: A perturbation approach. *Geophysics*. 2008;73(5):D63–D73. https://doi.org/10.1190/1.2921778.